A Novel Spatio-Temporal Frequency-Domain Imaging Technique for Two-Layer Materials Using Ultrasonic Arrays

NASIM MOALLEMI AND SHAHRAM SHAHBAZPANAHI, **(Senior Member, IEEE)**
Department of Electrical, Computer, and Software Engineering, University of Ontario Institute of Technology, Oshawa, ON L1H 7K4, Canada
Corresponding author: Shahram Shahbazpanahi (shahram.shahbazpanahi@uoit.ca)

ABSTRACT Ultrasonic imaging of multi-layer materials with parallel interfaces is a challenging problem in non-destructive testing. In multi-layer materials, since the sound velocity and the propagation path change when sound travels from one layer into another, calculating the sound travel time is complicated. In this paper, we develop a frequency-domain imaging algorithm for estimating the scattering coefficients of all the points inside the second layer of a two-layer (liquid-solid) medium in order to obtain an image of the region of interest. To do so, we first introduce our data model for the array received signals by modeling the interfaces between the layers of a two-layer medium as a spatially distributed source. Then, we introduce a mapping relationship between the two-dimensional image of the region of interest and the three-dimensional Fourier transform of the received signals. This proposed algorithm has relatively lower computational complexity and it can be used for online imaging. Computer simulations as well as experimental data show the accuracy of the proposed algorithm.

INDEX TERMS Distributed source, array signal processing, non-destructive testing, immersion ultrasonic imaging, multi-layer imaging.

I. INTRODUCTION

Non-destructive testing (NDT) includes a wide range of techniques which are used to evaluate the integrity of materials without causing any damage to them. Ultrasonic imaging is a popular NDT technique for imaging inside materials, such as pipelines, railways, and airplane parts. Indeed, ultrasonic imaging is a common method to inspect materials for flaw detection and thickness measurement in both industry and in medical diagnosis. Ultrasonic imaging uses high-frequency sound waves to detect any discontinuity inside the material under test. Ultrasonic inspection is attractive for NDT because it only needs to access one side of the materials under test. Moreover, it is highly accurate in localizing the scatterers and estimating the size and the shape of the flaws inside solid materials. Since 1980s, ultrasonic phased arrays have been drastically used for non-destructive testing in industry and medical diagnosis. The diversity provided by different positions of transmitters and receivers in an array of transducers facilitates localizing scatterers inside the material under test. Traditionally, ultrasonic arrays are used to emulate a monolithic transducer with a large aperture. Independent transmission circuits used for each transducer of the array

enable different transducers to fire with different time delays. Therefore, the probing sound wave can be focused on each point in the region of interest (ROI) within the sample under test to generate a real-time image. However, in many NDT applications, the targets are static and we can take advantage of off-line post-processing methods. To do so, the data corresponding to all combinations of transmitter and receiver transducers are collected in a matrix and are used in off-line post-processing. Larger coverage area without need for reconfiguration, improving sensitivity, and reducing the time for conducting the test, are some of the advantages of using transducer array compared to a conventional single-element transducer. The ultrasonic arrays used in NDT have different array geometries which are designed for different industrial applications. The maximum array size, which is currently used in NDT, is limited to 256 elements based on today's available computing power and electronic circuity size

In a test where an ultrasonic array is used, each transducer fires a sound wave while the other transducers, including the one transmitting, receive the signal backscattered from the material under test. Then, all the backscattered signals are collected in a three-dimensional tensor for post-processing.

This method is referred to as full matrix capture (FMC). There has been a considerable amount of research in the field of ultrasonic array imaging for NDT applications [1]–[8]. In most of these studies, it is assumed that the material under test is a homogeneous medium where the sound velocity is constant inside the material under test. Several algorithms have been proposed for imaging a homogeneous material including the plane B-scan, the sector B-scan, the focused B-scan, the total focusing method (TFM), and wavenumber algorithm [2]–[4]. All these algorithms rely on delay-and-sum beamforming technique which can be implemented either in time- or in frequency-domain. Among these algorithms, TFM, a time- domain algorithm for FMC, is easy to implement and is still used in many applications [3]. The wavenumber (ω-k) algorithm of [4] is a frequency-domain algorithm for FMC, which is popular because its execution time is considerably lower, compared to the TFM.

In many applications, the material under test is not homogeneous. One simple example is multi-layer material with parallel interfaces. Assuming a sound source located inside the first layer of a multi-layer medium, the sound wave is refracted into lower layers at the interfaces between the layers. As a result, the sound velocity and the shape of the wave front change when sound travels from one layer into another. Thus, in multi-layer materials, calculating the sound travel time is complicated.

Another example of multi-layer imaging is in immersion test in NDT, where a solid test object and a transducer array are immersed in water. In fact, the immersion ultrasonic inspection is preferred in many applications because of its speed and reliability advantages over the contact method, as discussed in [9]–[13]. Also, immersible transducers have wide bandwidths, ranging from low MHz to more than 10 MHz in water. Such wide-band transducers are of interest for many imaging applications, for example see [12].

There are a few algorithms proposed for multi-layer imaging, including the root-mean-square velocity based technique [14], [15], the phase shift migration (PSM) algorithm [9], and the multi-layer omega-k (MULOK) method [10]. The root-mean-square velocity technique was primarily proposed for seismology applications [14], [15]. In this technique, a weighted average velocity of the sound velocities in different earth's seismic layers is used to calculate the sound travel time through different layers. This method has also been used for ultrasonic biomedical imaging[1] in [23] and has been tested for two-layer NDT ultrasonic imaging in [11]. The RMS velocity approach is appropriate when the sound velocity is slightly different between the layers and it is not recommended when the sound velocities are significantly different in different layers. The PSM algorithm which was also originally proposed for seismic imaging, is applicable for imaging a multi-layer medium with parallel interfaces. In the PSM algorithm, the sound

wave at each depth in the material under test is extrapolated for a different depth by multiplying it with a unit-norm complex exponential factor in frequency domain. In [10], the MULOK algorithm, which is a combination of the PSM and the wavenumber (ω-k) algorithms, has been proposed, for multi-layer imaging. In the MULOK algorithm, the wavenumber algorithm is used for imaging each layer of a multi-layer medium, and the PSM algorithm is used to extrapolate the wave amplitude from each layer to another one. All the aforementioned three algorithms have been proposed for multi-layer imaging in a synthetic aperture focusing scenario, i.e., when a single transducer is used to emulate an array by repeating the test when the transducer is located at different positions. These algorithms have not been used for ultrasonic imaging when a real array of transducers is used. One idea for multi-layer array processing is time gating with a correction factor for the refraction between the layers. In [24], a modified version of TFM has been used for multi-layer ultrasonic imaging.

In [25], to avoid all the problems associated with a two-layer medium, the array is approximated with, and thus, can be replaced by an equivalent array which operates in the second medium only. Therefore, the two-layer problem is converted to a single-layer scenario. However, there are timing errors due to the approximation used in [25].

In all these aforementioned studies, the sound wave is treated as a plane wave, thus the refraction at the interface between two adjacent layers can be modeled using Snell's law. In many applications of ultrasonic imaging, the source transducer is located at a finite distance from the receiving transducer and the layer boundaries, thus the plane wave modeling is not accurate. An alternative approach is to model the sound wave as a non-planar (for example spherical or cylindrical) wave. To tackle the problem of refraction of a non-planar (for example spherical or cylindrical) wave at the interface between two media with two different velocities, in [26], we proposed an approach based on the Huygens-Fresnel principle. According to this principle, a wave field on a surface can determine the wave field off of that surface. More specifically, each point on the surface can be viewed as a source of a secondary wave. The superposition of these secondary sources on the surface determines the strength of the wave at any point off of that surface. This formulation leads to the Rayleigh-Sommerfeld integral. In [26], we used the Huygens' principle and Rayleigh-Sommerfeld integral over the interface between the two media and then, we developed a new array spatial signature for all points inside a two-layer liquid-solid (LS) medium. Then, we used this new array spatial signature in three different imaging techniques, namely the conventional beamforming technique, the MUSIC method, and the Capon algorithm, in order to image two-layer LS materials. These techniques belong to the class of spatial filtering methods which combine the sensor outputs linearly (as in conventional beamforming) or non-linearly fashion (as in MUSIC and Capon based methods) to create an image of the ROI.

---

[1]Indeed, ultrasonic imaging has numerous biomedical applications, see for example [16]–[22].

The authors of [27] also use Rayleigh-Summerfeld integral at the interface between the two layers of different materials to calculate the reflected and transmitted ultrasonic fields.

In this paper, we use an alternative data model to develop a Fourier transform based imaging algorithm to estimate the scattering coefficients of all the points inside the second layer of a two-layer LS medium in order to obtain an image of the region of interest. In this proposed algorithm, the execution time is considerably reduced compared to the three afore-mentioned algorithms in [26], and it can be used in an online imaging process.

Our method is indeed performed in the spatio-temporal frequency domain. That is, we work with the three dimensional signals in Fourier domain. These three dimensions include one temporal frequency dimension denoted as ω, and two spatial frequency dimensions represented by k_x and k_y. The major advantage of the proposed spatio-temporal frequency domain algorithm is its much simpler computational complexity. For large arrays and images, the proposed algorithm is several orders faster.

Note that at the interface of the two layers, mode conversion phenomenon happens whereby an incident wave is converted to two or more modes, each of which have different propagation velocity. Considering the mode conversion and the contribution of the shear wave in the received signal, makes the data model too complicated. To simplify the problem of interest, it is a common practice to assume that there is no mode conversion at the interface between the two layers. Indeed, this assumption is not out of place considering that the velocity of shear waves is about half of the velocity of the longitudinal waves, which means that the contributions from the two modes appear well separated in time, at least for deep reflectors, and hence, they can be separated from each other. Also, the transmittance for shear waves is very small compared with the longitudinal wave [9]–[11]. Also, commercially available ultrasonic arrays are not designed to receive shear wave. In this paper, we assume that the interference due to the presence of shear wave in the received signal as noise.

The remainder of this paper is organized as follows. In Section II, we introduce our data model for the array received signals using the concept of spatially distributed sources. In Section III, we introduce a mapping relationship between the two-dimensional image of the ROI and the three-dimensional tensor of frequency-domain received signals, which can be used to estimate the scattering coefficients of all the points inside the second layer of a two-layer LS medium. In Section IV, we present our algorithm for imaging the second layer of a two-layer LS medium. In Section V, we use computer simulations as well as experimental data to show the accuracy of the proposed algorithm. Finally, conclusions are drawn in Section VI.

II. DATA MODEL

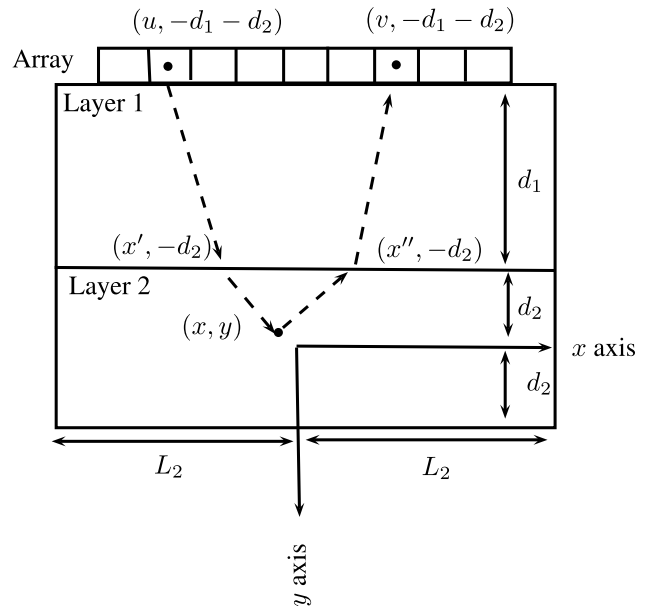We consider a solid object which is under ultrasonic immersion test using a one-dimensional uniform linear array

FIGURE 1. A hypothetical point scatterer inside second layer of a two-layer LS medium.

of M ultrasonic transducers.[2] We assume that each layer is a homogeneous medium with a constant sound velocity; however, the sound velocity in each layer is different from that in the other layer. Each transducer transmits a sound wave and all the other transducers (including the one transmitting) receive the sound wave backscattered from the test sample. The M^2 time domain received signals are sampled in time and stored in a $N \times M \times M$ tensor where N is the number of time samples. The goal is to develop a data model for the backscattered signals with the aim to use it for imaging the material under test.

We assume that the upper surface of the test sample, the interface between the layers, and the back wall of the test sample are parallel planes (i.e., we deal with a two-layer LS with parallel interfaces). The center of the two-dimensional Cartesian coordinate system is assumed to be in the middle of the second layer of the material under test, as shown in Fig. 1. The width of the first layer in y direction is d_1 and the width of the second layer in y direction is $2d_2$. We present our data model in a two-dimensional coordinate system, assuming that the ultrasonic transducers, the test sample, and the defects are infinitely long in the third dimension. This model can easily be extended for three-dimensional volumetric imaging scheme where a two-dimensional uniform array is employed. All the transducers in the array are assumed to be identical and with identical beam patterns gain.

In NDT, Fermat principle (Snell's law) is often used to model the behavior of planar wave at the planar interface between two materials. The Fermat principle focuses on the

---

[2]The forthcoming approach is proposed for the case of unifrom linear arrays, and it is not suitable for an arbitrary array. Note that linear ultrasonic arrays has many application in NDT.

problem of plane waves in layered media. In the theory of acoustic wave propagation, however, it is important to take into account that the sound reflector is located at a finite distance from the receiver as well as from the boundaries. The most simple example of this is the classical problem of the field of a point source in the presence of an interface between two homogeneous media. This example is a problem of spherical wave reflection and refraction and Fermat principle is not applicable in a straightforward manner. To study such a problem, we model the interface between the two layers as a spatially distributed source. Assuming a two-dimensional model, this interface can be modeled as a line consisting of infinite number of point sources [28]. At each point on the interface, the propagating sound wave is refracted into the second layer, therefore, each point on the interface acts as a point source for all the points inside the second layer. Let us assume that there is a point scatterer located at (x, y) inside the second layer of the test sample, and the transducer located at coordinate $(u, -d_1 - d_2)$ is firing the probing sound wave. This sound wave is refracted by all points on the interface between the two layers into the second layer. Then, any point scatterer scatters the sound wave back towards the interface. This backscattered sound wave is refracted into the first layer by all the points on the interface, and the transducer array measures the superposition of all these refracted signals. This superposition stems from the Huygens-Fresnel principle. According to this principle, a wave field on a surface can determine the wave field off of that surface. More specifically, each point on the surface can be viewed as a source of a secondary wave. The superposition of these secondary sources on the surface determines the strength of the wave at any point off of that surface.

Therefore, at frequency ω, in the absence of noise,[3] the backscattered signal received by the transducer located at coordinate $(v, -d_1 - d_2)$ due to the scattering of a point scatterer, located at (x, y) in the second layer is denoted by $p_{x,y}(\omega; u, v)$ and it can be written as [4], [26].

$$p_{x,y}(\omega; u, v)$$

$$= \phi(\omega) f_{12} f_{21} \iint\limits_{-\infty}^{+\infty} B(\omega; u, -d_1 - d_2; x', -d_2)$$

$$\times B(\omega; v, -d_1 - d_2; x'', -d_2,) s(x, y) \, g_f(\omega; x' - u, d_1)$$

$$\times g_s(\omega; x - x', y + d_2) g_s(\omega; x - x'', y + d_2)$$

$$\times g_f(\omega; x'' - v, d_1) dx' dx''. \qquad (1)$$

Here, $\phi(\omega)$ is the frequency-domain representation of the probing signal at frequency ω, f_{12} is the transmission coefficient from Layer 1 into Layer 2, f_{21} is the transmission coefficient from Layer 2 into Layer 1, $s(x, y)$ is the *real-valued* scattering coefficient of a hypothetical point scatterer located at (x, y) inside the second layer, $B(\omega; u, -d_1 - d_2; x', -d_2)$

---

[3]Noise can be simply added to our data model without affecting the model for the desired signal. Such additive noise can model all model imperfections as well as the interference caused due to the presence of shear wave in the received signal.

is the beam pattern gain of the source transducer, located at $(u, -d_1 - d_2)$, towards a point located at $(x', -d_2)$ on the interface at frequency ω, and $B(\omega; v, -d_1 - d_2; x'', -d_2,)$ is the beam pattern gain of the receiving transducer, located at $(v, -d_1 - d_2)$, for a point source located at $(x'', -d_2)$ on the interface at frequency ω. Also, $g_f(\omega; x' - u, d_1)$ is the Green function corresponding to the propagation of sound wave in the first layer from the source transducer, located at $(u, -d_1 - d_2)$, to a point located at $(x', -d_2)$ on the interface at frequency ω, $g_s(\omega; x - x', y + d_2)$ is the Green function corresponding to the propagation of sound wave in the second layer from a point located at $(x', -d_2)$ on the interface to a hypothetical point scatterer located at (x, y) inside the second layer at frequency ω, $g_s(\omega; x - x'', y + d_2)$ is the Green function corresponding to the propagation of sound wave in the second layer from a hypothetical point scatterer located at (x, y) inside the second layer to a point located at $(x'', -d_2)$ on the interface at frequency ω, and $g_f(\omega; x'' - v, d_1)$ is the Green function corresponding to the propagation of sound wave in the first layer from a point located at $(x', -d_2)$ on the interface to the receiving transducer located at $(v, -d_1 - d_2)$ at frequency ω. The Green functions in the first and second layers can be written, respectively, as [4], [29]

$$g_f(\omega; x, y) = \frac{-j}{4\pi} \int\limits_{-\infty}^{+\infty} \frac{\exp\left(-jk_x x - jy\sqrt{k_f^2 - k_x^2}\right)}{\sqrt{k_f^2 - k_x^2}} dk_x \quad (2)$$

$$g_s(\omega; x, y) = \frac{-j}{4\pi} \int\limits_{-\infty}^{+\infty} \frac{\exp\left(-jk_x x - jy\sqrt{k_s^2 - k_x^2}\right)}{\sqrt{k_s^2 - k_x^2}} dk_x. \quad (3)$$

Here, $k_f \triangleq \omega/c_f$ and $k_s \triangleq \omega/c_s$ are the wavenumbers in Layers 1 and 2, respectively, and c_f and c_s are the corresponding sound velocities in Layers 1 and 2.

Note that the exact value of the transmission coefficient f_{12} depends on the location of the refracting point on the interface and on the location of the hypothetical point scatterer. Also, the transmission coefficient f_{21} depends on the location of the refracting point on the interface and the location of the receiving transducer [29]. The exact values of the transmission coefficients f_{12} and f_{21} can be calculated using Huygens' principle as in [26]. However, the computational complexity of the approach proposed in [26] is relatively high. In this paper, to reduce the computational complexity, and consequently, the execution time, we assume that the transmission coefficients f_{12} and f_{21} are constant values across the interface between the two layers. With this assumption, we aim to propose an algorithm for ultrasonic imaging for two-layer LS materials.

In the backscattered signal, $p_{x,y}(\omega; u, v)$ depends on the probing signal $\phi(\omega)$, and the transducers beam-pattern gains $B(\omega; u, -d_1 - d_2; x', -d_2)$ and $B(\omega; v, -d_1 - d_2; x'', -d_2,)$. To further simplifying the model in (1), we assume that the probing signal is an impulse and that the transducers are omni-directional, i.e,

$$B(\omega; u, -d_1 - d_2; x', -d_2) = 1 \qquad (4)$$

$$B(\omega; v, -d_1 - d_2; x'', -d_2,) = 1 \tag{5}$$

$$\varphi(t) = \delta(t) \tag{6}$$

where $\varphi(t)$ is the time domain representation of $\phi(\omega)$. Alternatively, in practice, these effects can be compensated in the preprocessing steps [4]. Therefore, (1) can be written as

$$p_{x,y}(\omega; u, v) = f_{12} f_{21} \iint\limits_{-\infty}^{+\infty} s(x, y)\, g_f(\omega; x' - u, d_1)$$
$$\times g_s(\omega; x - x', y + d_2) g_s(\omega; x - x'', y + d_2)$$
$$\times g_f(\omega; x'' - v, d_1) dx' dx''. \tag{7}$$

Note that $p_{x,y}(\omega; u, v)$ is the received signal due to the scattering of only one point scatterer inside the second layer. Therefore, using superposition principle the backscattered signal, received at the transducer located at $(v, -d_1 - d_2)$ due to the scattering of all potential point scatterers in the ROI, can be written as

$$p(\omega; u, v) = f_{12} f_{21} \iint\limits_{-\infty}^{+\infty} \iint\limits_{-\infty}^{+\infty} s(x, y) g_f(\omega; x' - u, d_1)$$
$$\times g_s(\omega; x - x', y + d_2) g_s(\omega; x - x'', y + d_2)$$
$$\times g_f(\omega; x'' - v, d_1) dx' dx'' dx dy \tag{8}$$

Note that $s(x, y)$ may be non-zero only for those points in the ROI which reflect the sound wave.

III. FOURIER MAPPING

In this section, we use the data model in (8) to develop a relationship between the Fourier representation of the measured data $p(\omega; u, v)$ and the Fourier representation of the image $s(x, y)$, for all the points in the ROI.

Using (2) and (3), we can write (8) as

$$p(\omega; u, v)$$
$$= f_{12} f_{21} \iint\limits_{-\infty}^{+\infty} \iint\limits_{-\infty}^{+\infty} s(x, y) \frac{dx' dx'' dx dy}{(4\pi)^4}$$
$$\times \left(\int_{-\infty}^{+\infty} \frac{\exp\left(-jk_1(x' - u) - jd_1\sqrt{k_f^2 - k_1^2}\right)}{\sqrt{k_f^2 - k_1^2}} dk_1 \right)$$
$$\times \left(\int_{-\infty}^{+\infty} \frac{\exp\left(-jk_2(x - x') - j(y + d_2)\sqrt{k_s^2 - k_2^2}\right)}{\sqrt{k_s^2 - k_2^2}} dk_2 \right)$$
$$\times \left(\int_{-\infty}^{+\infty} \frac{\exp\left(-jk_3(x - x'') - j(y + d_2)\sqrt{k_s^2 - k_3^2}\right)}{\sqrt{k_s^2 - k_3^2}} dk_3 \right)$$
$$\times \left(\int_{-\infty}^{+\infty} \frac{\exp\left(-jk_4(x'' - v) - jd_1\sqrt{k_f^2 - k_4^2}\right)}{\sqrt{k_f^2 - k_4^2}} dk_4 \right). \tag{9}$$

We now rewrite (9) as in (10), as shown at the bottom of the next page. Let $S(k_x, k_y)$ denote the two-dimensional Fourier transform of $s(x, y)$, that is

$$S(k_x, k_y) \triangleq \iint\limits_{-\infty}^{+\infty} s(x, y) \exp\left(-jxk_x - jyk_y\right) dxdy. \tag{11}$$

Using (11), we can write

$$\iint\limits_{-\infty}^{+\infty} s(x, y) \exp\left(-jx(k_2+k_3)-jy(\sqrt{k_s^2 - k_2^2} + \sqrt{k_s^2 - k_3^2})\right)$$
$$\times dxdy = S\left(k_2 + k_3, \sqrt{k_s^2 - k_2^2} + \sqrt{k_s^2 - k_3^2}\right). \tag{12}$$

We now use (12) to write (10) as in (13), as shown at the bottom of the next page. To simplify (13), we define $Z(w, k_2, k_3)$ as

$$Z(\omega; k_2, k_3) \triangleq \frac{\exp\left(-jd_2(\sqrt{k_s^2 - k_2^2} + \sqrt{k_s^2 - k_3^2})\right)}{\sqrt{k_s^2 - k_2^2}\sqrt{k_s^2 - k_3^2}}$$
$$\times S\left(k_2 + k_3, \sqrt{k_s^2 - k_2^2}+\sqrt{k_s^2 - k_3^2}\right) \tag{14}$$

Therefore, we have the following relationships between $Z(w, k_2, k_3)$ and its two-dimensional inverse Fourier transform which is denoted as $z(w, x', x'')$:

$$z(\omega; x', x'') \triangleq \frac{1}{2\pi} \iint\limits_{-\infty}^{+\infty} \exp(jx'k_2+jx''k_3)Z(\omega; k_2, k_3)dk_2dk_3 \tag{15}$$

$$Z(\omega; k_2, k_3) \triangleq \iint\limits_{-\infty}^{+\infty} \exp(-jx'k_2-jx''k_3)z(\omega, x', x'')dx' dx''. \tag{16}$$

Using (14), we can write (13) as in (17), as shown at the bottom of the next page. Then using (15), we can write (17) as in (18). Based on the definition in (16), we can write

$$Z(\omega; k_1, k_4)$$
$$= \frac{1}{2\pi} \times \iint\limits_{-\infty}^{+\infty} \exp(-jx'k_1 - jx''k_4)z(\omega, x', x'')dx' dx''. \tag{19}$$

Therefore, using (19), we can write (18), as shown at the bottom of the next page, as in (20), as shown at the bottom of the next page. Then, seeking the similarity with the definition of inverse Fourier transform, we write (20) as in (21), as shown at the bottom of the next page. We now define $P(\omega; k_1, k_4)$ as the two-dimensional Fourier transform of $p(\omega; u, v)$ as

$$P(\omega; k_1, k_4) \triangleq \frac{1}{2\pi} \iint\limits_{-\infty}^{+\infty} \exp(-jk_1u - jk_4v)p(\omega; u, v)dk_1dk_4. \tag{22}$$

$$p(\omega; u, v) = \frac{f_{12} f_{21}}{(4\pi)^4} \iint_{-\infty}^{+\infty} \frac{\exp\left(jk_1 u + jk_4 v - jd_1 \left(\sqrt{k_f^2 - k_1^2} + \sqrt{k_f^2 - k_4^2}\right)\right)}{\sqrt{k_f^2 - k_1^2}\sqrt{k_f^2 - k_4^2}}$$

$$\times \left[\iint_{-\infty}^{+\infty} \exp(-jx'k_1 - jx''k_4) \left[\iint_{-\infty}^{+\infty} \exp(jx'k_2 + jx''k_3) \frac{\exp\left(-jd_2\left(\sqrt{k_s^2 - k_2^2} + \sqrt{k_s^2 - k_3^2}\right)\right)}{\sqrt{k_s^2 - k_2^2}\sqrt{k_s^2 - k_3^2}}\right.\right.$$

$$\times \left.\left.\left[\iint_{-\infty}^{+\infty} s(x, y) \exp\left(-jx(k_2 + k_3) - jy\left(\sqrt{k_s^2 - k_2^2} + \sqrt{k_s^2 - k_3^2}\right)\right) dx\,dy\right] dk_2 dk_3\right] dx'dx''\right] \times dk_1 dk_4 \quad (10)$$

$$p(\omega; u, v) = \frac{f_{12} f_{21}}{(4\pi)^4} \iint_{-\infty}^{+\infty} \frac{\exp\left(jk_1 u + jk_4 v - jd_1 \left(\sqrt{k_f^2 - k_1^2} + \sqrt{k_f^2 - k_4^2}\right)\right)}{\sqrt{k_f^2 - k_1^2}\sqrt{k_f^2 - k_4^2}}$$

$$\times \left[\iint_{-\infty}^{+\infty} \exp(-jx'k_1 - jx''k_4) \left[\iint_{-\infty}^{+\infty} \exp(jx'k_2 + jx''k_3) \frac{\exp\left(-jd_2\left(\sqrt{k_s^2 - k_2^2} + \sqrt{k_s^2 - k_3^2}\right)\right)}{\sqrt{k_s^2 - k_2^2}\sqrt{k_s^2 - k_3^2}}\right.\right.$$

$$\times \left.\left. S\left(k_2 + k_3, \sqrt{k_s^2 - k_2^2} + \sqrt{k_s^2 - k_3^2}\right) dk_2 dk_3\right] dx'dx''\right] dk_1 dk_4 \quad (13)$$

$$p(\omega; u, v) = \frac{f_{12} f_{21}}{(4\pi)^4} \iint_{-\infty}^{+\infty} \frac{\exp\left(jk_1 u + jk_4 v - jd_1 \left(\sqrt{k_f^2 - k_1^2} + \sqrt{k_f^2 - k_4^2}\right)\right)}{\sqrt{k_f^2 - k_1^2}\sqrt{k_f^2 - k_4^2}}$$

$$\times \left[\iint_{-\infty}^{+\infty} \exp(-jx'k_1 - jx''k_4) \left[\iint_{-\infty}^{+\infty} \exp(jx'k_2 + jx''k_3)Z(\omega; k_2, k_3)dk_2 dk_3\right] dx'dx''\right] dk_1 dk_4. \quad (17)$$

$$p(\omega; u, v) = \frac{f_{12} f_{21}}{2(4\pi)^3} \iint_{-\infty}^{+\infty} \frac{\exp\left(jk_1 u + jk_4 v - jd_1 \left(\sqrt{k_f^2 - k_1^2} + \sqrt{k_f^2 - k_4^2}\right)\right)}{\sqrt{k_f^2 - k_1^2}\sqrt{k_f^2 - k_4^2}}$$

$$\times \left[\iint_{-\infty}^{+\infty} \exp(-jx'k_1 - jx''k_4)z(\omega; x', x'')dx'dx''\right] dk_1 dk_4. \quad (18)$$

$$p(\omega; u, v) = \frac{f_{12} f_{21}}{2(4\pi)^3} \iint_{-\infty}^{+\infty} \frac{\exp\left(jk_1 u + jk_4 v - jd_1 \left(\sqrt{k_f^2 - k_1^2} + \sqrt{k_f^2 - k_4^2}\right)\right)}{\sqrt{k_f^2 - k_1^2}\sqrt{k_f^2 - k_4^2}} Z(\omega; k_1, k_4)dk_1 dk_4. \quad (20)$$

$$p(\omega; u, v) = \frac{1}{2\pi} \iint_{-\infty}^{+\infty} \exp(jk_1 u + jk_4 v) \left(\frac{f_{12} f_{21} Z(\omega; k_1, k_4) \exp\left(-jd_1 \left(\sqrt{k_f^2 - k_1^2} + \sqrt{k_f^2 - k_4^2}\right)\right)}{4(4\pi)^2 \sqrt{k_f^2 - k_1^2}\sqrt{k_f^2 - k_4^2}}\right) dk_1 dk_4. \quad (21)$$

Using (21) and (22), we can write

$$P(\omega; k_1, k_4)$$
$$= \frac{f_{12}f_{21}Z(\omega; k_1, k_4) \exp\left(-jd_1\left(\sqrt{k_f^2 - k_1^2} + \sqrt{k_f^2 - k_4^2}\right)\right)}{4(4\pi)^2 \sqrt{k_f^2 - k_1^2}\sqrt{k_f^2 - k_4^2}}.$$
$$(23)$$

Therefore, $Z(\omega; k_1, k_4)$ can be written as

$$Z(\omega; k_1, k_4)$$
$$= \frac{4(4\pi)^2 \sqrt{k_f^2 - k_1^2}\sqrt{k_f^2 - k_4^2}\, P(\omega; k_1, k_4)}{f_{12}\, f_{21}\, \exp\left(-jd_1\left(\sqrt{k_f^2 - k_1^2} + \sqrt{k_f^2 - k_4^2}\right)\right)}. \quad (24)$$

Using (24) and (14), we can write

$$S\left(k_1 + k_4, \sqrt{k_s^2 - k_1^2} + \sqrt{k_s^2 - k_4^2}\right) = H(\omega; k_1, k_4) \quad (25)$$

where $H(\omega; k_1, k_4)$ is given as in (26), as shown at the bottom of this page.

In the next section, we show how this relationship can be used to obtain $s(x, y)$ from the $P(\omega; k_1, k_4)$. Note that (25) and (26) describe a mapping relationship between the Fourier transform of $s(x, y)$ and the Fourier transform of $p(\omega; u, v)$. If we consider noise in (1), the noise will go under the same transformation in (25) and (26).

IV. IMAGING ALGORITHM
In this section, we aim to present an algorithm for imaging the second layer of a two-layer LS medium using the data model we obtained in the previous section. To do so, we first compute the three-dimensional Fourier transform of the time-domain array received signals, denoted by $\tilde{p}(t, u, v)$ to obtain $P(\omega; k_1, k_4)$, where k_1 and k_4 are the spatial frequency variables associated with the spatial coordinate u and v, respectively.

In the second step, using the following variable mapping,

$$k_x = k_1 + k_4 \quad (27)$$
$$k_y = \sqrt{k_s^2 - k_1^2} + \sqrt{k_s^2 - k_4^2}, \quad (28)$$

we can write (25) as

$$S(k_x, k_y) = H(\omega; k_1, k_4), \quad (29)$$

which shows how we can obtain $S(k_x, k_y)$ from $H(\omega; k_1, k_4)$. The transformation in (29) shows how the three-dimensional data $H(\omega; k_1, k_4)$ can be transformed into the two-dimensional Fourier representation $S(k_x, k_y)$ of the image $s(x, y)$. To apply this transformation, we hold k_1 constant and for each constant k_1, we can estimate the $S(k_x, k_y)$. We denote the estimate of the $S(k_x, k_y)$ corresponding to k_1, as $\hat{S}(k_x, k_y|k_1)$ and it can be written as [4]

$$\hat{S}(k_x, k_y|k_1) = H(\omega; k_1, k_4)\Big|_{\substack{k_4 = k_x - k_1 \\ \omega = k_s c_s}} \quad (30)$$

where k_s is obtained as

$$k_s = \frac{\pm\sqrt{\left(k_y^4 + 2\left(k_1^2 + k_4^2\right)k_y^2 + k_1^4 + k_4^4 - 2k_1^2 k_4^2\right)}}{2k_y}. \quad (31)$$

Indeed, $\hat{S}(k_x, k_y|k_1)$ is an estimate of $S(k_x, k_y)$ corresponding to a given value of k_1. To eliminate the affect of noise on the

image, we take average of $\hat{S}(k_x, k_y|k_1)$ over all the values of k_1 as [4]

$$\tilde{S}(k_x, k_y) = \int_{-\infty}^{+\infty} \hat{S}(k_x, k_y|k_1) dk_1 \quad (32)$$

where $\tilde{S}(k_x, k_y)$ is the average of all estimate values of $S(k_x, k_y)$ over all the values of k_1. As we assumed that $s(x, y)$ is real, the $\tilde{S}(k_x, k_y)$ for the negative values of k_y can be written as

$$\hat{S}(k_x, -k_y) = \hat{S}^*(-k_x, k_y) \quad k_y > 0 \quad (33)$$

where $*$ is the complex conjugate operator. Now, having $S(k_x, k_y)$ for all the values of k_x and k_y, we take two-dimensional inverse Fourier transform of $\hat{S}(k_x, k_y)$ to obtain $\hat{s}(x, y)$ which is introduced as the image of the ROI.

V. SIMULATION AND EXPERIMENTAL RESULTS
In this section, we evaluate the accuracy of our proposed data model and the proposed algorithm for imaging the second layer of a two-layer LS medium. As mentioned earlier, one of the applications of two-layer imaging is immersion ultrasonic test. In an immersion ultrasonic test, the ultrasonic transducers and the test sample are immersed in a liquid such as water, thereby coupling the probing sound wave from the transducers to the material under test. We conducted an immersion ultrasonic test using a uniform linear array of ultrasonic transducers. In our experiment, we used a 64-element Olympus uniform linear array (5L64-I1). Therefore, all the parameter values correspond to this immersion probe. The ultrasonic array is placed in water above a steel test sample. The ultrasonic array probe is parallel to the upper surface of the test sample. The center of the array is assumed to be located at $x = 0$ mm and $y = 27.5$ mm. The test configuration is depicted in Fig 1. The space between the array probe and the test sample is $d_1 = 9.5$ mm which is filled by water. When one of the transducers fires a probing sound wave, the sound wave travels through two homogeneous materials including water and steel. The goal is to image the steel test sample which acts as the second layer of a two-layer LS medium.

The ultrasonic transducer array consists of $M = 64$ elements. Each transducer has a rectangular shape, and is 0.6 mm wide (in x direction) and 10 mm long (in z direction). Therefore, the transducers are long enough (i.e., 10 mm $\gg$ 0.6 mm) to be considered as long linear sources which produce cylindrical sound waves. The distance between the center of any two adjacent transducers (element pitch) is 0.6 mm amounting an active aperture of 38.4 mm. The

$$H(\omega; k_1, k_4) = \frac{P(\omega; k_1, k_4)\sqrt{k_f^2 - k_1^2}\sqrt{k_f^2 - k_4^2}\sqrt{k_s^2 - k_1^2}\sqrt{k_s^2 - k_4^2}}{\exp\left(-jd_2(\sqrt{k_s^2 - k_1^2} + \sqrt{k_s^2 - k_4^2})\right)\exp\left(-jd_1\left(\sqrt{k_f^2 - k_1^2} + \sqrt{k_f^2 - k_4^2}\right)\right)} \quad (26)$$

material under test is a steel block with five drilled-sided-holes. The test sample is a homogeneous medium with a width of 160 mm (in x direction) and a height of 36 mm (in y direction), and a length of 20 mm (in z direction). The holes are drilled all the way through the length of the test sample (in z direction). We assume that the holes are long linear secondary sources which produce backscattered cylindrical sound waves. The holes are considered as defects to be localized using ultrasonic immersion test. The velocity of the sound wave inside the test sample was measured to be approximately 6300 m/s. Also, the velocity of the sound wave in water is assumed to be 1480 m/s. The velocity of sound in the metal and water was measured by the time of sound travel in water and metal using the backscattered signal of the upper and lower surface of the test sample.

The ultrasonic transducers produce longitudinal sound wave, and we have ignored the production of shear wave in the mode conversion phenomenon. Each transducer fires a probing sound wave toward the test sample through the water, and other transducers receive the backscattered sound wave from the test sample. There is enough time delay between the firing adjacent transducers to avoid any undesired interference between firing subsequence transducers. The 4096 time-domain received signals are sampled with appropriate sampling frequency and stored in a $64 \times 64 \times 5000$ tensor for post-processing. The sampling frequency is $F_s = 100$ MHz and the number of samples, N is 5000. To avoid multi-path interference signals, we process only the first 2400 samples of all the received signals. Also, the first 1400 samples, corresponding to the propagation of the sound wave in the first layer are replaced with zero. The probing signal is a wide-band signal with a center frequency of 5 MHz. To suppress the noise, the high frequency components are replaced with zero. In the other words, we filter the signal using a low pass filter. In Fig. 3a, we have shown the image of the material under test using our proposed imaging algorithm using 1320 frequency bins. The three-dimensional version of this image is shown in Fig. 3c. The ROI is the area between the lines $x = -40$ mm, and $x = 40$ mm, and $y = -18$ mm, $y = 18$ mm corresponding to the steel test sample according to the coordinate system shown in Fig. 2. All the images have been normalized to their maximum values (brightest pixel in the image). The three prominent peaks belong to Holes A, B, and C, which are shown in Fig. 2.

We also image the steel block (the second layer of the two-layer LS medium of water and steel) using the single-layer wavenumber algorithm of [4]. To do so, we have chosen the part of the signal corresponding to the propagation of the sound in the steel block using time gating. To this end, the time samples between 1400 and 2400 have been chosen. These samples correspond to the wave reflected from all points in the second layer, which are calculated based on the aforementioned sound velocities in the two layers. Using the single-layer wavenumber algorithm of [4], in Fig. 3b, we have shown the image of the steel test sample. The three-dimensional version of this image is shown
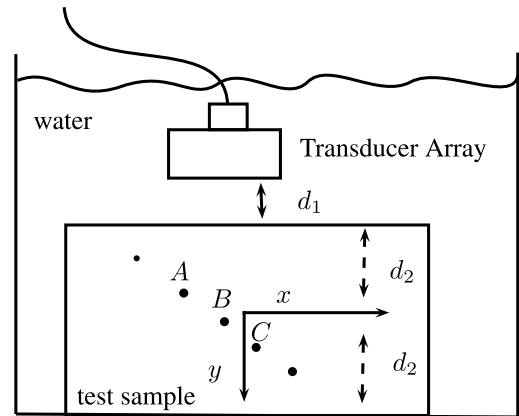

FIGURE 2. Test configuration.

in Fig. 3d. The peaks in Fig. 3a and Fig. 3c, obtained using our proposed algorithms are more prominent in comparison to peaks in Fig. 3b and Fig. 3d obtained using single-layer wavenumber algorithm [4] in conjunction with time-gating. To better compare these two approaches, we have shown the images of Holes A, B, and C, in Fig. 4. These images clearly show that our proposed algorithm outperforms the single-layer wavenumber algorithm. Indeed, these two figures show that the shapes of the holes in our images are clearly closer to a circle while the shapes of the holes obtained by using the single-layer wavenumber algorithm of [4] are far from a circle.

The performance of the proposed algorithm in terms of the cut-off frequency in the low-pass filter (or equivalently the number of frequency bins chosen from the Fourier representation of the signal) is investigated in Fig. 5. We can see from these images that as we increase the number of frequency bins or the cut-off frequency of the low-pass filter, the peaks are more prominent leading to more clearer images. However, increasing the number of frequency bins will increase the computational complexity of the algorithm. That is, there is a trade-off between the image clarity and computational complexity.

To evaluate the performance of our proposed method, in terms of root mean squared error (RMSE), we now provide an RMSE plot versus the SNR. To do so, we have added a zero-mean Gaussian noise with different powers, corresponding to different values of SNR, to the raw data. Note that here the SNR is defined as the power of the additive noise to the power of the backscattered signal at the receiving transducers. We reconstruct the image using the data contaminated with additive noise and calculate the RMSE of the location of the peaks. The RMSE is calculated based on the assumption that the true location of the peak in the image is the one which is obtained from the original data (without additive noise). Using 1320 frequency bins, Fig. 6 shows the RMSEs for the holes' location estimates obtained using different methods including the proposed method, the single-layer wavenumber algorithm of [4], the RMS velocity based approach of [11], and our earlier work in [26].
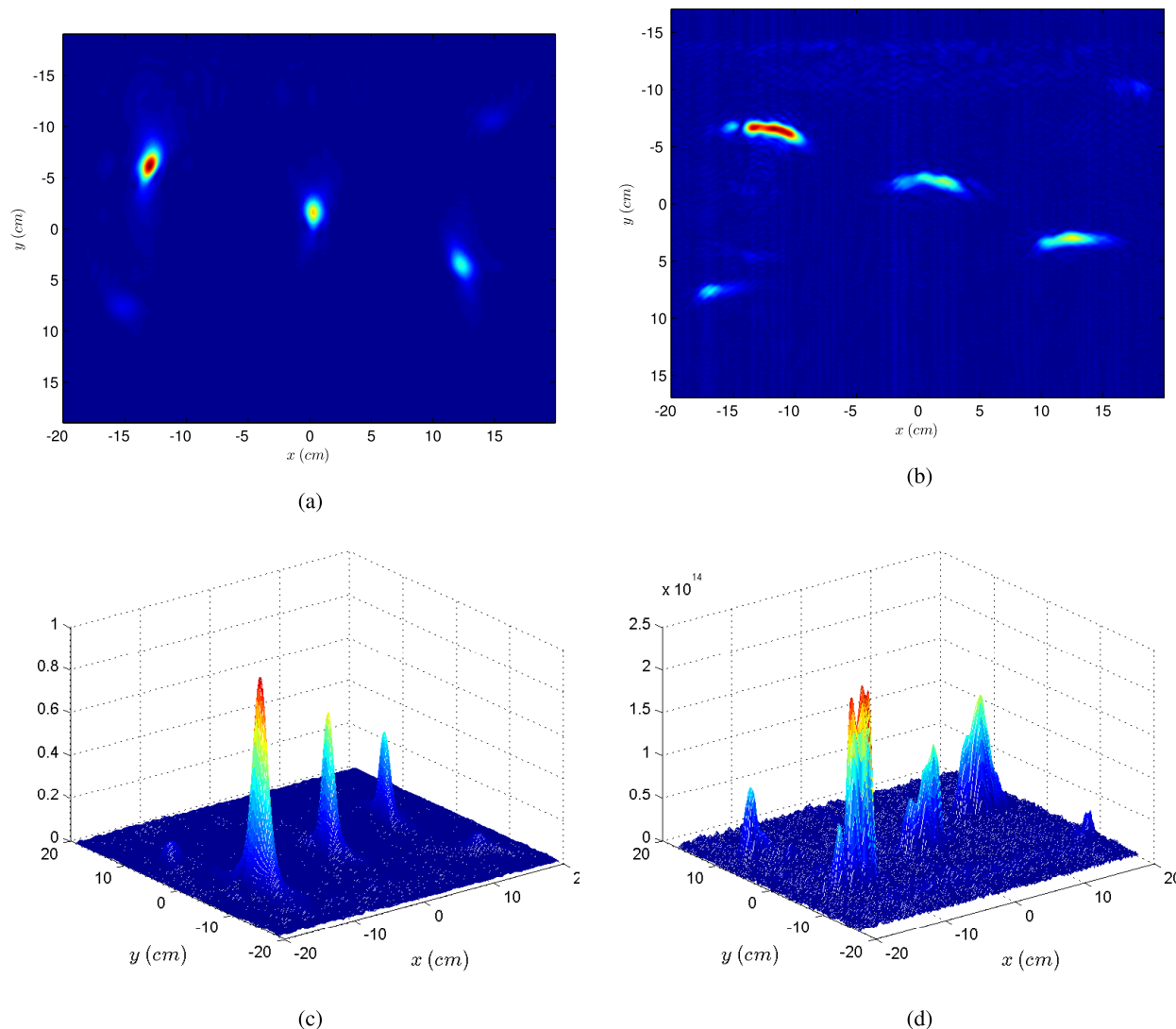
FIGURE 3. A comparison between our proposed algorithm and the single-layer wavenumber algorithm. (a) Image of the ROI obtained using the proposed algorithm. (b) Image of the ROI obtained using the single-layer wavenumber algorithm. (c) Three-dimensional plot obtained using the proposed algorithm. (d) Three-dimensional plot obtained using the single-layer wavenumber algorithm.

This figure clearly shows the superiority of the proposed method compared to the single-layer wavenumber algorithm and the RMS velocity based approach, while showing a only slight performance degradation compared to the method of [26]. Note however that the computational complexity of the method of [26] is prohibitively high, and thus, the proposed method offers an alternative low complexity solution at a negligible performance loss. This slightly better performance of the method of [26] stems from the fact that this method uses the knowledge of the fired pulse shape in the frequency domain to build the corresponding image. Hence, in those frequencies where this pulse has low energy, the contribution of the data in those frequencies to the image will be relatively low. However, in the proposed method, based on (6), the pulse shape is assumed to be flat in frequency domain. Such an assumption is only an approximation to the true shape of the pulse.

We now comment on the computational complexity of the proposed algorithm. Considering an array of M ultrasonic transducers, the M^2 time domain received signals are sampled in time and stored in a $N \times M \times M$ tensor, where N is the number of time samples. In the proposed Fourier-based imaging technique, the computational cost of the 3-D FFT is $\mathcal{O}(M^2 N \log(M^2 N))$. Then each 2-D slice of the Fourier transformed data is interpolated into an $L \times K$ image. This interpolation has a computational complexity of $\mathcal{O}(LKM)$. Then a 2-D inverse FFT is applied to each of these $L \times K$ images (a total of M images) with a total computational complexity of $\mathcal{O}(MLK \log(LK))$. Therefore, the computational cost is $\mathcal{O}(LKM + MLK \log(LK) + M^2 N \log(M^2 N))$. This computational complexity is the same as that of the wavenumber algorithm. However, as shown through our numerical simulations, our proposed technique outperforms the wavenumber technique. Compared to the techniques studied in [26], our
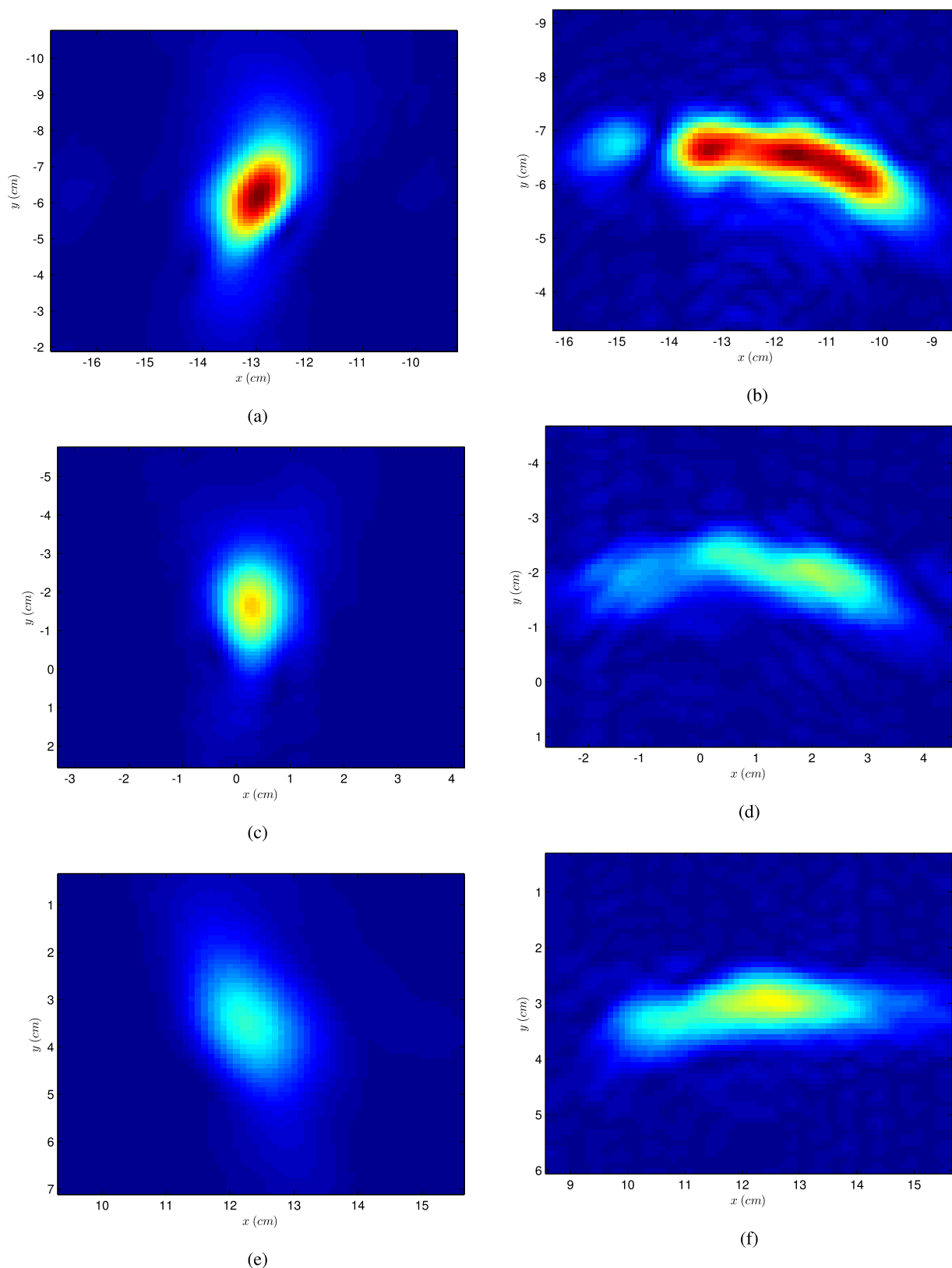
FIGURE 4. Images of the Holes A, B, and C using our proposed algorithm and for the single-layer wavenumber algorithm. (a) Image of hole A obtained using the proposed algorithm. (b) Image of hole A obtained using the single-layer wavenumber algorithm. (c) Image of hole B obtained using the proposed algorithm. (d) Image of hole B obtained using the single-layer wavenumber algorithm. (e) Image of hole C obtained using the proposed algorithm. (f) Image of hole C obtained using the single-layer wavenumber algorithm.
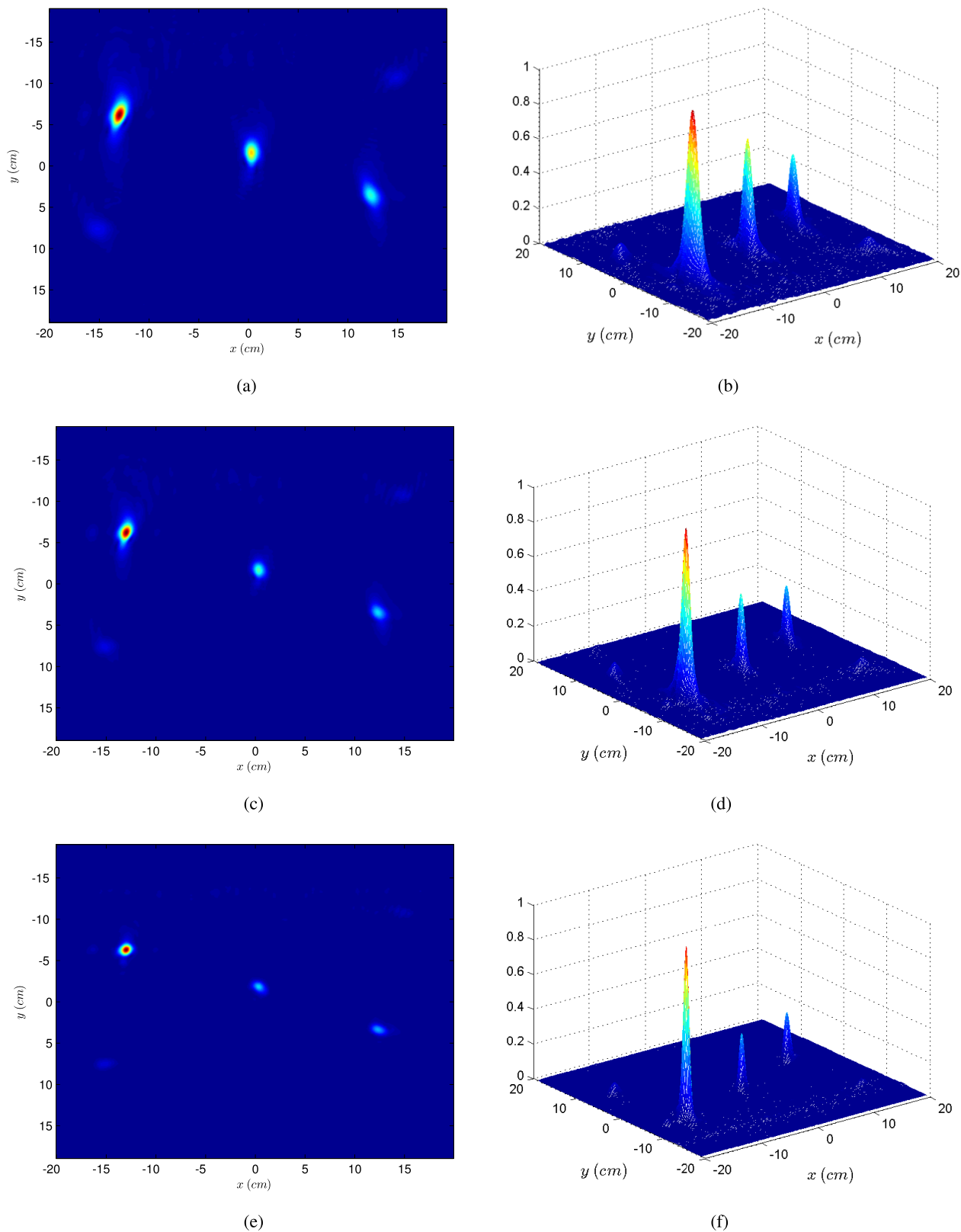
FIGURE 5. Image of the ROI using our proposed algorithm for different number of frequency bins. (a) Image of the ROI using 1320 frequency bins. (b) Three-dimensional image of ROI using 1320 frequency bins. (c) Image of the ROI using 1350 frequency bins. (d) Three-dimensional image of ROI using 1350 frequency bins. (e) Image of the ROI using 1400 frequency bins. (f) Three-dimensional image of ROI using 1400 frequency bins.
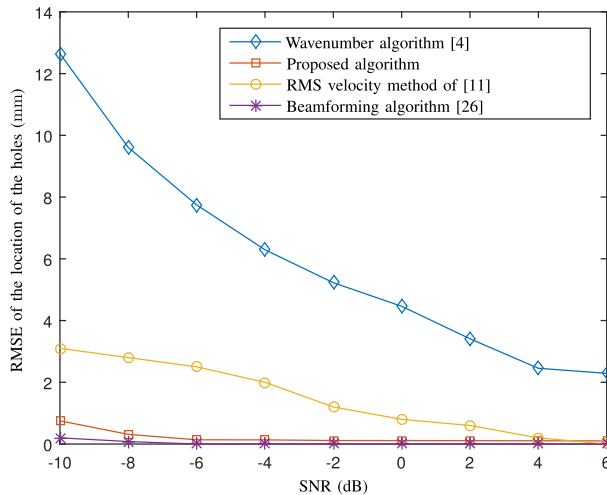
FIGURE 6. The RMSE curves versus SNR.

algorithm is much faster. The reason is that calculating the model introduced in [26] for array spatial signature involves approximating a certain integral using numerical techniques. While the computational complexities of these numerical techniques are not easily quantifiable, one can say that to ensure an accurate approximation of the aforementioned integral, number of points in the corresponding numerical approximation has to be to sufficiently large and this results in a very high computational complexity for the algorithms of [26]. Our proposed scheme trades off imaging performance to gain computational advantage over the methods of [26], see [30] for more details.

VI. CONCLUSIONS

In this paper, we used the distributed source modeling approach for the interface between the layers of a two-layer LS medium. Then, we developed a Fourier transform based imaging algorithm to estimate the scattering coefficients of all the points inside the second layer of a two-layer LS medium in order to obtain an image of the region of interest (ROI). This algorithm is based on a mapping relationship which we establish between the two-dimensional image of the ROI and the three-dimensional frequency-domain backscattered signals. In this proposed algorithm, the computational complexity is relatively low, and it can be used in an online imaging process. Computer simulations as well as experimental data show the accuracy of the proposed algorithm.

REFERENCES

[1] B. W. Drinkwater and P. D. Wilcox, "Ultrasonic arrays for non-destructive evaluation: A review," *NDT E Int.*, vol. 39, no. 7, pp. 525–541, Oct. 2006.

[2] C. Holmes, B. W. Drinkwater, and P. D. Wilcox, "Post-processing of the full matrix of ultrasonic transmit–receive array data for non-destructive evaluation," *NDT E Int.*, vol. 38, pp. 701–711, Dec. 2005.

[3] P. D. Wilcox, C. Holmes, and B. W. Drinkwater, "Advanced reflector characterization with ultrasonic phased arrays in NDE applications," *IEEE Trans. Ultrason., Ferroelect., Freq. Control*, vol. 54, no. 8, pp. 1541–1550, Aug. 2007.

[4] A. J. Hunter, B. W. Drinkwater, and P. D. Wilcox, "The wavenumber algorithm for full-matrix imaging using an ultrasonic array," *IEEE Trans. Ultrason., Ferroelect., Freq. Control*, vol. 55, no. 11, pp. 2450–2462, Nov. 2008.

[5] F. Lingvall and T. Olofsson, "On time-domain model-based ultrasonic array imaging," *IEEE Trans. Ultrason., Ferroelect., Freq. Control*, vol. 54, no. 8, pp. 1623–1633, Aug. 2007.

[6] T. Stepinski, "An implementation of synthetic aperture focusing technique in frequency domain," *IEEE Trans. Ultrason., Ferroelect., Freq. Control*, vol. 54, no. 7, pp. 1399–1408, Jul. 2007.

[7] M. H. Skjelvareid, Y. Birkelund, and Y. Larsen, "Synthetic aperture focusing of outwardly directed cylindrical ultrasound scans," *IEEE Trans. Ultrason., Ferroelect., Freq. Control*, vol. 59, no. 11, pp. 2460–2469, Nov. 2012.

[8] M. H. Skjelvareid, Y. Birkelund, and Y. Larsen, "Internal pipeline inspection using virtual source synthetic aperture ultrasound imaging," *NDT E Int.*, vol. 54, pp. 151–158, Mar. 2013.

[9] T. Olofsson, "Phase shift migration for imaging layered objects and objects immersed in water," *IEEE Trans. Ultrason., Ferroelect., Freq. Control*, vol. 57, no. 11, pp. 2522–2530, Nov. 2010.

[10] M. H. Skjelvareid, T. Olofsson, Y. Birkelund, and Y. Larsen, "Synthetic aperture focusing of ultrasonic data from multilayered media using an omega-K algorithm," *IEEE Trans. Ultrason., Ferroelect., Freq. Control*, vol. 58, no. 5, pp. 1037–1048, May 2011.

[11] M. Skjelvareid and Y. Birkelund, "Ultrasound imaging using multi-layer synthetic aperture focusing," in *Proc. ASME*. Bellevue, WA, USA, Jul. 2010, pp. 379–387.

[12] J. S. McIntosh, D. A. Hutchins, D. R. Billson, R. A. Noble, R. R. Davies, and L. Koker, "SAFT imaging using immersed capacitive micromachined ultrasonic transducers," in *Proc. Ultrason. Symp.*, vol. 2. Oct. 2002, pp. 1019–1022.

[13] T. Olofsson, M. H. Skjelvareid, and A. Barkefors, "Ultrasonic imaging of immersed objects using migration techniques," in *Proc. Eur. Conf. Synth. Aperture Radar (EUSAR)*, Jun. 2010, pp. 1–4.

[14] W. A. Schneider, "The common depth point stack," *Proc. IEEE*, vol. 72, no. 10, pp. 1238–1254, Oct. 1984.

[15] P. S. Schultz, "Seismic velocity estimation," *Proc. IEEE*, vol. 72, no. 10, pp. 1330–1339, Oct. 1984.

[16] T. Araki *et al.*, "A comparative approach of four different image registration techniques for quantitative assessment of coronary artery calcium lesions using intravascular ultrasound," *Comput. Methods Programs Biomed.*, vol. 118, no. 2, pp. 158–172, 2015.

[17] L. Saba *et al.*, "Automated stratification of liver disease in ultrasound: An online accurate feature classification paradigm," *Comput. Methods Programs Biomed.*, vol. 130, pp. 118–134, Jul. 2016.

[18] N. Ikeda *et al.*, "Improved correlation between carotid and coronary atherosclerosis SYNTAX score using automated ultrasound carotid bulb plaque IMT measurement," *Ultrasound Med. Biol.*, vol. 41, no. 5, pp. 1247–1262, 2015.

[19] K. Sharma and J. Virmani, "A decision support system for classification of normal and medical renal disease using ultrasound images: A decision support system for medical renal diseases," *Int. J. Ambient Comput. Intell.*, vol. 8, no. 2, pp. 52–69, 2017.

[20] S. S. Chavan and S. N. Talbar, "Multimodality medical image fusion using M-band wavelet and Daubechies complex wavelet transform for radiation therapy," *Int. J. Rough Sets Data Anal.*, vol. 2, no. 2, pp. 1–23, 2015.

[21] T. Araki *et al.*, "Link between automated coronary calcium volumes from intravascular ultrasound to automated carotid IMT from B-mode ultrasound in coronary artery disease population," *J. Int. Union Angiol.*, vol. 33, no. 4, pp. 392–440, 2014.

[22] A. M. Anter, M. A. El Souod, A. T. Azar, and A. E. Hassanien, "A hybrid approach to diagnosis of hepatic tumors in computed tomography images," *Int. J. Rough Sets Data Anal.*, vol. 1, no. 2, pp. 31–48, 2014.

[23] M. A. Haun, D. L. Jones, and W. D. O'Brien, "Adaptive focusing through layered media using the geophysical 'time migration' concept," in *Proc. Ultrason. Symp.*, Munich, Germany, vol. 2. Feb. 2002, pp. 1635–1638.

[24] P. D. Wilcox, "Ultrasonic arrays in NDE: Beyond the B-scan," in *Proc. Amer. Inst. Phys. (AIP) Conf.*, 2013, pp. 33–50.

[25] J. F. Cruza, J. Camacho, L. Serrano-Iribarnegaray, and C. Fritsch, "New method for real-time dynamic focusing through interfaces," *IEEE Trans. Ultrason., Ferroelect., Freq. Control*, vol. 60, no. 4, pp. 739–751, Apr. 2013.

[26] N. Moallemi and S. Shahbazpanahi, "A new model for array spatial signature for two-layer imaging with applications to nondestructive testing using ultrasonic arrays," *IEEE Trans. Signal Process.*, vol. 63, no. 10, pp. 2464–2475, May 2015.

[27] F. Buiochi, O. Martinez, L. Gomez-Ullate, and F. M. D. Espinosa, "A computational method to calculate the longitudinal wave evolution caused by interfaces between isotropic media," *IEEE Trans. Ultrason., Ferroelect., Freq. Control*, vol. 51, no. 2, pp. 181–192, Feb. 2004.

[28] N. Moallemi and S. Shahbazpanahi, "A distributed reflector localization approach to ultrasonic array imaging in non-destructive testing applications," *IEEE Trans. Signal Process.*, vol. 62, no. 15, pp. 3863–3873, Aug. 2014.

[29] J. W. Goodman, *Introduction to Fourier Optics*. New York, NY, USA: McGraw-Hill, 1996.

[30] N. Moallemi, "Ultrasonic array imaging for multi-layer materials in non-destructive testing applications," Ph.D. dissertation, Univ. Ontario Inst. Technol., Oshawa, ON, Canada, Dec. 2014.

NASIM MOALLEMI received the M.Sc. degree in electrical engineering with a major in telecommunications from Shiraz University in 2009, and the Ph.D. degree in electrical engineering from the University of Ontario Institute of Technology, Oshawa, Canada. Her current research interest includes ultrasonic array imaging for nondestructive testing applications. She is currently a Lecturer at the Department of Electrical, Computer, and Software Engineering, University of Ontario Institute of Technology, Oshawa, Canada.

SHAHRAM SHAHBAZPANAHI (M'02–SM'10) was born in Sanandaj, Iran. He received the B.Sc., M.Sc., and Ph.D. degrees in electrical engineering from the Sharif University of Technology, Tehran, Iran, in 1992, 1994, and 2001, respectively. From 1994 to 1996, he was a faculty member with the Department of Electrical Engineering, Razi University, Kermanshah, Iran. From 2001 to 2003, he was a Post-Doctoral Fellow with the Department of Electrical and Computer Engineering, McMaster University, Hamilton, ON, Canada. From 2003 to 2004, he was a Visiting Researcher with the Department of Communication Systems, University of Duisburg-Essen, Duisburg, Germany. From 2004 to 2005, he was a Lecturer and an Adjunct Professor with the Department of Electrical and Computer Engineering, McMaster University. In 2005, he joined the Faculty of Engineering and Applied Science, University of Ontario Institute of Technology, Oshawa, ON, Canada, where he currently holds a full Professor position. His research interests include statistical and array signal processing, space-time adaptive processing, detection and estimation, multi-antenna, multi-user, and cooperative communications, spread spectrum techniques, DSP programming, and hardware/real-time software design for telecommunication systems. He also served as an elected member of the Sensor Array and Multichannel Technical Committee of the IEEE Signal Processing Society. He received several awards, including the Early Researcher Award from the Ontario's Ministry of Research and Innovation, the NSERC Discovery Grant (three awards), the Research Excellence Award from the Faculty of Engineering and Applied Science and the Research Excellence Award, Early Stage, from the University of Ontario Institute of Technology. He has served as an Associate Editor for the IEEE Transactions on Signal Processing and the IEEE Signal Processing Letters. He served as a Senior Area Editor for the IEEE Signal Processing Letters.

• • •